

2022

## A Local Mode Study of Ring Puckering Effects in the Infrared Spectra of Cyclopentane

Edwin L. Sibert III  
*University of Wisconsin-Madison*

Peter F. Bernath  
*Old Dominion University, pbernath@odu.edu*

Follow this and additional works at: [https://digitalcommons.odu.edu/chemistry\\_fac\\_pubs](https://digitalcommons.odu.edu/chemistry_fac_pubs)

 Part of the [Atomic, Molecular and Optical Physics Commons](#), [Organic Chemistry Commons](#), and the [Thermodynamics Commons](#)

---

### Original Publication Citation

Sibert, E. L., III., & Bernath, P. F. (2022). A local mode study of ring puckering effects in the infrared spectra of cyclopentane. *The Journal of Chemical Physics*, 156(21), 1-13, Article 214305. <https://doi.org/10.1063/5.0095010>

This Article is brought to you for free and open access by the Chemistry & Biochemistry at ODU Digital Commons. It has been accepted for inclusion in Chemistry & Biochemistry Faculty Publications by an authorized administrator of ODU Digital Commons. For more information, please contact [digitalcommons@odu.edu](mailto:digitalcommons@odu.edu).

# A local mode study of ring puckering effects in the infrared spectra of cyclopentane

Cite as: J. Chem. Phys. 156, 214305 (2022); doi: 10.1063/5.0095010

Submitted: 7 April 2022 • Accepted: 9 May 2022 •

Published Online: 2 June 2022



View Online



Export Citation



CrossMark

Edwin L. Sibert III<sup>1,a)</sup>  and Peter F. Bernath<sup>2,3</sup> 

## AFFILIATIONS

<sup>1</sup> Department of Chemistry and Theoretical Chemistry Institute, University of Wisconsin-Madison, Madison, Wisconsin 53706, USA

<sup>2</sup> Department of Chemistry and Biochemistry, Old Dominion University, Norfolk, Virginia 23529, USA

<sup>3</sup> Department of Physics, Old Dominion University, Norfolk, Virginia 23529, USA

<sup>a)</sup> Author to whom correspondence should be addressed: [elsibert@wisc.edu](mailto:elsibert@wisc.edu)

## ABSTRACT

We report and interpret recently recorded high-resolution infrared spectra for the fundamentals of the CH<sub>2</sub> scissors and CH stretches of gas phase cyclopentane at  $-26.1$  and  $-50$  °C, respectively. We extend previous theoretical studies of this molecule, which is known to undergo barrierless pseudorotation due to ring puckering, by constructing local mode Hamiltonians of the stretching and scissor vibrations for which the frequencies, couplings, and linear dipoles are calculated as functions of the pseudorotation angle using B3LYP/6-311++(d,p) and MP2/cc-pVTZ levels of theory. Symmetrization ( $D_{5h}$ ) of the vibrational basis sets leads to simple vibration/pseudorotation Hamiltonians whose solutions lead to good agreement with the experiment at medium resolution, but which miss interesting line fractionation when compared to the high-resolution spectra. In contrast to the scissor motion, pseudorotation leads to significant state mixing of the CH stretches, which themselves are Fermi coupled to the scissor overtones.

Published under an exclusive license by AIP Publishing. <https://doi.org/10.1063/5.0095010>

## I. INTRODUCTION

The cyclopentane molecule has unusual thermodynamic,<sup>1</sup> spectroscopic,<sup>2–6</sup> and dynamical properties<sup>4–7</sup> as a result of ring puckering. This puckering leads to a low frequency internal motion known as pseudorotation.<sup>8,9</sup> Motion along this, essentially barrierless motion, includes ten distinct “bent” conformers and ten distinct “twist” conformers. Accurate rotational, rovibrational coupling, and centrifugal distortion constants for this degree of freedom have been very accurately determined by femtosecond time-resolved Raman rotational coherence spectroscopy.<sup>7</sup>

The article by Kowalewski *et al.*<sup>7</sup> provides a nice review of previous studies as well as an excellent description of pseudorotation in cyclopentane. The present study extends that work by developing a theoretical model that describes how pseudorotation couples the CH<sub>2</sub> scissor and CH stretch vibrations. Our study is guided by our high-resolution infrared gas phase spectra of the fundamentals of these vibrations that are reported herein. The CH<sub>2</sub> scissor spectrum improves upon the resolution of the corresponding spectrum recorded by Bauman and Laane.<sup>3</sup> Our theory also extends the

treatment of those workers who were able to describe the main features of this spectral region with a one-dimensional particle in a ring model of pseudorotation combined with the appropriate selection rules.

The C–H stretch region of the infrared spectrum of most hydrocarbons consists of many unresolved transitions in the spectral region 2900–3000 cm<sup>−1</sup>. This complexity is due to multiple CH stretch transitions from multiple conformers that are all perturbed by Fermi resonances with first overtones and combination modes of CH<sub>2</sub> scissors vibrations. Over the last ten years, the Zwier and Sibert groups<sup>10–13</sup> have combined experiment with theory to study these vibrations for molecules in ground and excited states for both open and close shell systems. These molecules include phenyl groups, which allow one to record single conformer spectra under molecular beam conditions by infrared-ultraviolet double resonance.

More recently, we have applied these models as part of our analysis of high-resolution infrared spectra of several molecules of astrochemical interest. These molecules include isobutane,<sup>14</sup> neopentane,<sup>15</sup> and cyclohexane.<sup>16</sup> The key feature of the model is a set of harmonically coupled local mode CH stretches and CH<sub>2</sub>

scissor motions combined with linear dipole moment operators. All parameters are calculated with electronic structure methods. To obtain spectroscopic accuracy,<sup>12</sup> the alkyl CH stretch and CH<sub>2</sub> scissor frequencies are scaled by the factors 0.960 and 0.975, respectively, and the harmonic local modes are dressed with anharmonic couplings that have been found to be insensitive to the level of theory and specific stretch-bend environments.

In this article, we extend these models to include coupling to pseudorotation motion of cyclopentane. Building on previous work,<sup>3,7</sup> we obtain local mode Hamiltonians describing both the “bent” and “twist” conformers and then use symmetry to infer how the Hamiltonians and dipole matrix elements depend on the pseudorotation coordinate. These results are combined with a particle in a ring basis set and a variational calculation to obtain vibrational spectra. Expressing the vibrational contribution of this direct product basis in a  $D_{5h}$  symmetric representation leads to Hamiltonians that take on surprisingly simple forms that allows us to interpret key spectral features.

Both the Raman and infrared selection rules of cyclopentane have been worked out by Mills.<sup>17</sup> That work employs an adiabatic representation in which a high frequency CH<sub>2</sub> scissor normal mode is coupled to the pseudorotation coordinate. This representation provides an excellent zero order picture. If, however, one wants to include the couplings between the normal coordinates, there are disadvantages of this representation. These modes, which are close in energy, are functions of the pseudorotation angle. This dependence can lead to complex non-adiabatic effects that require careful analysis. For example, Dawadi and Perry<sup>18</sup> reported seven conical intersections in the adiabatic treatment of the CH stretch normal modes interacting with the torsional degree of freedom in methanol in their description of the CH fundamental region of the IR spectrum. For this reason, we use a diabatic basis consisting of localized modes. These modes have only minor changes in frequency and character during the pseudorotation. Consequently, non-adiabatic effects are small and can be neglected.

The structure of this paper is as follows: We begin by describing the experimental methods in Sec. II. Pseudorotation in cyclopentane is reviewed in Sec. III. In Sec. IV, we develop the Hamiltonian and dipole moment operators for the CH<sub>2</sub> scissor motions coupled to pseudorotation. In Sec. V, we provide a parallel description for the CH stretches coupled to the pseudorotation. Section VI includes results and discussion. Our conclusions are presented in Sec. VII.

## II. EXPERIMENTAL METHODS

The cyclopentane spectra were recorded using the same apparatus and methods as used previously for cyclohexane.<sup>16</sup> Briefly, spectra in two regions were recorded with our high-resolution Bruker Fourier transform spectrometer using an internal 20 cm cold cell with wedged CaF<sub>2</sub> windows. For the C–H stretching region, 1.47 Torr of cyclopentane at  $-50^{\circ}\text{C}$  was used, and for the CH<sub>2</sub> scissors, the sample temperature was  $-26.1^{\circ}\text{C}$  at 25.8 Torr pressure. The CH stretching spectrum was used an InSb detector, and the resolution was  $0.02\text{ cm}^{-1}$ ; a HgCdTe detector was used for the CH<sub>2</sub> region at a resolution of  $0.01\text{ cm}^{-1}$ . These data were preliminary spectra and additional spectra were subsequently recorded to determine the infrared absorption cross sections.<sup>19</sup>

## III. PSEUDOROTATION

There are two nonequivalent structures involved in the pseudorotation of cyclopentane.<sup>1,3,7</sup> These structures are referred to as the “bent” and “twist” structures, and two representative conformers are shown in Fig. 1. These structures are similar to those of the  $D_{5h}$  geometry and can be thought of as distortions from that higher symmetry geometry.

If the  $z$ -axis is taken as the fivefold rotation axis, and the carbon atoms ordered 1–5 as one moves around the ring in the clockwise direction with carbon atom 1 situated on the positive  $y$ -axis, then the stable, lower symmetry conformers can be distinguished by the distortion of the carbon atoms out of the  $x, y$  plane of the molecule.

Following the earlier work of Kowalewski *et al.*,<sup>7</sup> the ring diagrams of Fig. 2 illustrate these distortions as one moves along the pseudorotation coordinate  $\phi$ . The distinct “bent” and “twist” structures are labeled as  $b_n^{\pm}$  and  $t_n^{\pm}$ , where  $n$  runs from 1 to 5. The definition of  $\phi$  follows from the recognition<sup>1</sup> that the progression through the structures of Fig. 2 can be modeled as

$$z_k = \left(\frac{2}{5}\right)^{1/2} q \cos\left(\frac{4\pi}{5}(k-1) + 2\phi\right), \quad (1)$$

where  $z_k$  is the out-of-plane displacement coordinate of the  $k$ th carbon atom as numbered in Fig. 1. The radial coordinate  $q$  describes the amplitude of the out-of-plane puckering. Two dimensional plots  $V(q, \phi)$  indicate that these two coordinates are weakly coupled.<sup>3,7</sup> Consequently, pseudorotation can be modeled assuming  $q = q_e$ .<sup>1,3,7</sup>

The motion along the pseudorotation coordinate  $\phi$  is essentially barrierless<sup>3,7</sup> and can be modeled with a one-dimensional particle in a ring Hamiltonian. The resulting eigenvalues

$$E_{\text{rot}} = B_{\phi} \ell^2 \quad (2)$$

are described by the quantum numbers  $\ell = 0, \pm 1, \pm 2, \dots, \pm \infty$ . The value of  $B_{\phi}$  has been determined to be  $2.8\text{ cm}^{-1}$  by femtosecond time-resolved Raman rotational coherence spectroscopy.<sup>7</sup> Bauman and Laane<sup>3</sup> consider modifications of this formula in the presence of coupling to the radial coordinate  $q$ . These correction terms are beyond the scope of the current work.

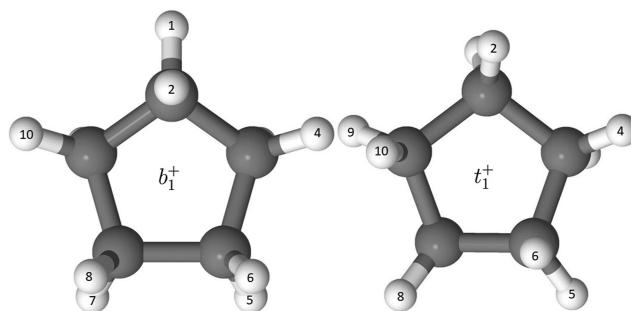


**FIG. 1.** Plot of the “bent”  $b_1^+$  and “twist”  $t_1^+$  structure showing the numbering scheme for the H atom and the equatorial and axial environments of the CH<sub>1</sub> and CH<sub>2</sub> stretches, respectively. The carbon atoms are numbered 1–5 (not shown) clockwise with atom 1 at the top. Structures are calculated at the B3LYP/6-311++(d,p) level of theory with the “bent” being  $0.9\text{ cm}^{-1}$  more stable than the “twist” conformer.

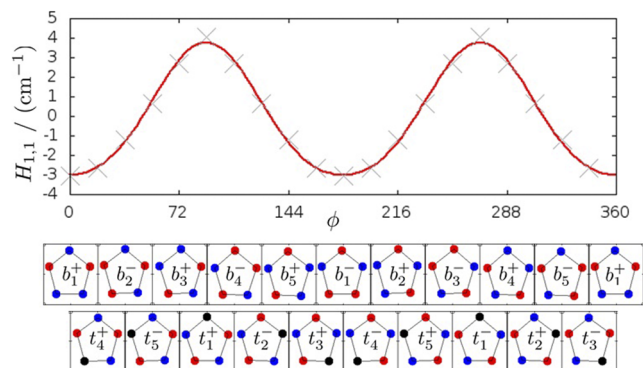


**FIG. 2.** The fluctuations of the  $H_{1,1}$  matrix elements for the  $\text{CH}_2$  scissor mode associated with carbon 1 plotted as a function of the pseudorotation angle  $\phi$ . Its average value is  $a_{0,0}$ . The conformations are shown below as a function of  $\phi$ . The top atom is carbon 1 with the remaining increasing in a clockwise direction. The blue circles have positive  $z$  values, red circles have negative  $z$  values, and black circles are  $z = 0$ . The crosses correspond to local mode results at each of the 10 equilibrium  $b_n^\pm$  and transition state  $t_n^\pm$  geometries ( $n = 1-5$ ). The above labeling follows the notation of Kowalewski *et al.*<sup>7</sup>

Despite the fact that motion along this coordinate is barrierless, there are interesting structural changes. As an example, the  $\text{H}_1$  and  $\text{H}_2$  atoms for the  $b_1^+$  geometry of Fig. 1 are approximately in the equatorial and axial positions. However, after a pseudorotation of  $180^\circ$  these positions are flipped. In this study, we build on these concepts to create scissor and stretch Hamiltonians and dipoles as functions of the angle  $\phi$  and then couple them to particle in a ring states associated with pseudorotation.

#### IV. $\text{CH}_2$ SCISSOR VIBRATIONS

We begin by focusing on the form of the coupling between the scissor and pseudorotation modes. The goal is to express the coupling in a form that allows for transparent expressions for the Hamiltonian matrix elements in a direct product representation.

##### A. Hamiltonian

Following our earlier works we describe the scissors and stretches using a localized representation of the vibrations.<sup>12,14,20,21</sup> The Reiher *et al.*<sup>22,23</sup> realized that, for molecules for which there are a number of characteristic bands consisting of close-lying delocalized normal modes, one can carry out an orthogonal transformation of these select modes and obtain a new set of modes that describe spatially localized vibrations. The localization can be carried out in several ways,<sup>22-27</sup> but we have found that, for CH stretches and  $\text{CH}_2$  scissors, the results are insensitive to the details of the localization. Our localization approach<sup>21</sup> requires a single mass scaling parameter that allows us to construct an intermediate set of normal modes in which spatial localization of vibrations is achieved by scaling select atomic masses by a factor of  $\gamma$ . Details of this method are described in the work of Sibert<sup>21</sup> and not repeated here. The starting point of the approach is a Hessian calculated with the Gaussian suite<sup>28</sup> at the B3LYP/6-311++(d,p) level of theory. Localizing the scissor modes

for the  $b_1^+$  conformer, shown in Fig. 2, leads to the following  $5 \times 5$  scissor Hamiltonian matrix:

$$\mathbf{H} = \begin{pmatrix} 1497.2 & 5.3 & 5.0 & 5.0 & 5.3 \\ 5.3 & 1499.0 & 7.7 & 2.6 & 6.6 \\ 5.0 & 7.7 & 1502.8 & 10.4 & 2.6 \\ 5.0 & 2.6 & 10.4 & 1502.8 & 7.7 \\ 5.3 & 6.6 & 2.6 & 7.7 & 1499.0 \end{pmatrix}. \quad (3)$$

The above results were calculated with  $\gamma = 2.3$ , but  $\gamma$  values between 1.8 and 2.8 lead to changes of the above matrix elements by less than  $0.005 \text{ cm}^{-1}$ . Based on the  $b_1^+$  geometry of Fig. 2, one expects modes 2 and 5 to have the same frequencies. Likewise, modes 3 and 4 should have identical frequencies. The above Hamiltonian is consistent with those expectations.

Our work relies on a matrix representation rather than coordinates. We note that the matrix approach approximates the normal mode treatment; the off-diagonal quadratic terms in the local coordinates, which lead to the above off-diagonal elements in the matrix representation, also lead to couplings between states with three total quanta of scissor excitation. Since the energy differences between these states and the fundamentals is large compared to the couplings, the neglect of these off-resonant couplings is small, and we ignore them. Diagonalization of the above matrix leads to the eigenvalues  $E_i$  that agree with the Gaussian frequency results<sup>28</sup> to within  $0.2 \text{ cm}^{-1}$ . This excellent agreement justifies our approximation of the eigenfunctions of localized matrix representation being equivalent to the normal modes.

An important feature of the above Hamiltonian is that the off-diagonal elements are comparable to the energy differences between the diagonal elements. As a result, the eigenfunctions of the above matrix will depend sensitively on all the elements of the matrix. As the molecule undergoes pseudorotation, all these elements change, and hence the normal modes will also change. One can define the normal modes as functions of the pseudorotation angle<sup>17</sup> following an adiabatic separation of the low frequency pseudorotation and high frequency scissor vibrations, but one may still need to include nonadiabatic couplings between the closely spaced scissor states. We will see that this is certainly the case for the CH stretches of cyclopentane. The adiabatic approach<sup>18,29</sup> has proven successful in the treatment of the CH stretch normal modes interacting with the torsional degree of freedom in methanol. However, these approaches require that one is careful with geometrical phases, due to the presence of conical intersections.

The pseudorotation shown in Fig. 2 leads to equivalent structures, and, hence, the Hamiltonian matrices for all of the  $b_n^\pm$  structures can be constructed from Eq. (3) by keeping track of the equivalent structures. For example, the value of the  $H_{11}(\phi)$  matrix element, which is  $1497.2 \text{ cm}^{-1}$  for the  $\phi = 0$   $b_1^+$  structure, is equal  $1502.8 \text{ cm}^{-1}$  for  $\phi = 2\pi/5$ . At this angle, the molecule has the  $b_3^+$  geometry, and, based on Fig. 2, the  $H_{11}$  element of this conformer is equivalent to the  $H_{44}$  element of the  $b_1^+$  conformer. This information, when combined with the matrices associated with the “twist” geometries, allows us to construct Hamiltonian matrices for all the conformers shown in Fig. 2.

The top panel of Fig. 2 shows the  $\phi$  dependence for the variation of the  $H_{1,1}$  elements. The simple cosine dependence is clearly evident. A least squares fit with a cosine series,

$$H_{1,1}(\phi) = a_{0,0} + \frac{1}{2} \sum_{n=1}^2 a_{0,n} \cos(2in\phi), \quad (4)$$

is shown as the solid red line; the agreement is excellent. The expansion coefficients have two subscripts. The significance of the leading subscript will become apparent when we consider off-diagonal elements. The values of the fit coefficients, calculated at the B3LYP/6-311++(d,p) level of theory, are shown in Table I, as well as select results for an MP2 calculation with a larger basis set. Those couplings follow the same patterns for both calculations. The biggest difference is the  $a_{0,0}$  term that is scaled in our work.

Generalizing the above ideas, the elements of the  $5 \times 5$  scissor Hamiltonian matrix can be described using

$$H_{k,k'}(\phi) = \frac{1}{2} \sum_{n=0}^2 a_{j,n} \left[ e^{2in\phi} f_k^{-n} f_{k'}^{-n} + c.c. \right], \quad (5)$$

where  $j = |k' - k|$  and

$$f_k \equiv e^{i(k-1)\phi_{10}}, \quad (6)$$

with  $\phi_{10} = 2\pi/10$ . The exponential form of the  $\phi$  dependence of the expansion allows for easy evaluation of the particle in a ring matrix elements employed to treat pseudorotation degree of freedom.

One can rationalize the form of Eq. (5) by first recognizing that for the  $H_{1,1}$  element this equation is that of a Fourier expansion in the angle  $\phi$ . The remaining diagonal elements are written by shifting the origin of the expansion. As an example, the  $H_{2,2}$  is written as a Fourier expansion in terms of angle  $(\phi - \phi_{10})$ .

Given the fivefold cyclic symmetry of this molecule, it is convenient to work in a symmetrized basis  $\psi_{\ell_v}$ , expressed as

$$\psi_{\ell_v} = \sum_{j=1}^5 U_{\ell_v,j} \chi_j, \quad (7)$$

**TABLE I.** Expansion coefficients for the scissor Hamiltonian in wavenumbers ( $\text{cm}^{-1}$ ) [see Eq. (5)].

$j$	$a_{j,0}$	$a_{j,1}$	$a_{j,2}$
B3LYP/6-311++(d,p)			
0	1500.160	-3.327	0.366
1	7.256	-2.648	0.410
2	4.353	2.168	0.070
3	4.353	-2.168	0.070
4	7.256	2.648	0.410
MP2/cc-pVTZ			
0	1506.32	-3.94	0.09
1	7.46	-3.05	0.73
2	4.44	2.41	0.11

where

$$U_{\ell_v,k} = \exp[i\ell_v(k-1)\phi_5]/\sqrt{5} = f_k^{2\ell_v}/\sqrt{5}, \quad (8)$$

where  $\phi_5 \equiv 2\pi/5$ . Here, the  $\chi_j$  are the localized scissor modes. With this definition the symmetrized Hamiltonian takes the form

$$\mathcal{H} = \mathbf{U}^* \mathbf{H} \mathbf{U}^T. \quad (9)$$

The symmetrized representation leads to a diagonal Hamiltonian matrix for the  $D_{5h}$  scissor Hamiltonian. These states are labeled with the quantum number  $\ell_v$  that runs from  $-2$  to  $2$ . States with  $\ell_v = \pm 2$  have  $e_2'$  symmetry, states with  $\ell_v = \pm 1$  have  $e_1'$  symmetry, and the state with  $\ell_v = 0$  has  $a_1'$  symmetry.

If we use the notation  $c_n \equiv \exp[in\phi]$ , we can express the Hamiltonian in the compact form

$$\mathcal{H} = \begin{pmatrix} h_{11} & h_{12}c_2 & h_{13}c_4 & h_{14}c_4^* & h_{15}c_2^* \\ h_{21}c_2^* & h_{22} & h_{23}c_2 & h_{24}c_4 & h_{25}c_4^* \\ h_{31}c_4^* & h_{32}c_2^* & h_{33} & h_{34}c_2 & h_{35}c_4 \\ h_{41}c_4 & h_{42}c_4^* & h_{43}c_2^* & h_{44} & h_{45}c_2 \\ h_{51}c_2 & h_{52}c_4 & h_{53}c_4^* & h_{54}c_2^* & h_{55} \end{pmatrix}, \quad (10)$$

where

$$\mathbf{h} = \begin{pmatrix} 1491.1 & -2.6 & 0.3 & -0.1 & 3.2 \\ -2.6 & 1497.6 & -3.1 & 0.7 & -0.1 \\ 0.3 & -3.1 & 1523.4 & -3.1 & 0.3 \\ -0.1 & 0.7 & -3.1 & 1497.6 & -2.6 \\ 3.2 & -0.1 & 0.3 & -2.6 & 1491.1 \end{pmatrix}. \quad (11)$$

The form of this Hamiltonian allows for ready evaluation of the Hamiltonian matrix in a product basis of symmetrized scissor states and pseudorotation states  $\Phi_{\ell}(\phi) = \exp[i\ell\phi]/\sqrt{2\pi}$ . Using Eqs. (10) and (11), these elements are

$$\langle \ell_v, \ell + 2j | \mathcal{H} | \ell_v, \ell \rangle = \langle \ell + 2j | \mathcal{H}_{\ell_v, \ell_v'} | \ell \rangle = h_{\ell_v, \ell_v'} \delta_{\ell, \ell'}. \quad (12)$$

Here,  $\ell_t = \text{mod}(2\ell_v + \ell, 5)$  is a symmetry label. States with different values of  $\ell_t$  cannot couple. We will see below that the value of  $\ell_t$  partially distinguishes the vibration/pseudorotation symmetry.

We consider two examples to clarify the form of the Hamiltonian. If one considers the elements  $\ell' = \ell$ , then  $j = 0$  and the only nonzero terms are the diagonal terms

$$\langle \ell | \mathcal{H}_{\ell_v, \ell_v'} | \ell \rangle = h_{\ell_v, \ell_v}. \quad (13)$$

As a second example, consider the evaluation of the coupling between two states with  $\ell_t = 4$ ,

$$\langle -2 | \mathcal{H}_{-2,2} | 0 \rangle = 3.2 \text{ cm}^{-1}. \quad (14)$$

Note that the  $\{-2, 2\}$  elements corresponds to  $h_{15}$  in Eq. (11).

In summary, the Hamiltonian of Eq. (10) combined with the particle in a ring contribution of Eq. (2), allows one to solve for the scissor/pseudorotation eigenstates. The specific values of the

elements are derived from the density functional theory (DFT) calculations described above where the input data are calculations on one “bent” and one “twist” conformer. The eigenvalues are converged by increasing the maximum magnitude of the  $\ell$  quantum numbers that are included in the direct product basis. We chose an upper limit of  $\ell = \pm 18$  based on thermal accessibility; this value leads to a basis of 185 functions. An examination of the eigenfunctions, shows that in all cases one can accurately describe the eigenstates with fewer than four basis functions, so one could use much smaller basis sets.

## B. Dipoles

The  $\phi$ -dependent dipole matrix elements are determined following similar considerations as those for generating the Hamiltonian. The dipoles for the local scissors of the  $b_1^+$  conformer are reported in Table II. These values are the values of the matrix elements  $\mu_{i\alpha} = \langle 0|\mu_\alpha|\chi_i\rangle$  that couple the ground state to the local mode states of Eq. (3). We calculate the intensities (km/mol) for each conformer as

$$I_j = \sum_\alpha |\langle 0|\mu_\alpha|\Psi_j\rangle|^2 E_j. \quad (15)$$

Here,  $E_j$  ( $\text{cm}^{-1}$ ) and  $\Psi_j$  are the eigenvalues and eigenvectors of  $\mathbf{H}$  of Eq. (3). The missing constants in the above expression are included in our units of the dipole matrix elements that have dimensions  $\sqrt{\text{km/mol/cm}^{-1}}$ . The dipole matrix elements are obtained as

$$\langle 0|\mu_\alpha|\Psi_j\rangle = \sum_{i=1}^5 \langle 0|\mu_\alpha|\chi_i\rangle \langle \chi_i|\Psi_j\rangle. \quad (16)$$

The resulting  $E_j$  and  $I_j$ , reported in Table II, agree closely with the results of Gaussian<sup>28</sup> with the intensities agreeing to within 0.01 km/mol.

The dipole components for the first scissor mode are shown as a function of  $\phi$  in Fig. 3. Also shown are fits to these results. The  $x$  and  $y$  components are fit as constants, with the former having a value of zero and the latter having a value of  $d_{y0} = -0.03278$ . The  $z$ -axis component, to a good approximation, can be fit as  $\mu_{1z}(\phi) = d_{z1} \cos(\phi)$  with  $d_{z1} = -0.03832$ . A striking feature of these results is that the  $y$ -component only has a weak  $\phi$  dependence.

**TABLE II.** Dipole matrix elements<sup>a</sup> of local scissors for the  $b_1^+$  conformer along with scissor excitation energies ( $\text{cm}^{-1}$ ) and intensities  $I_j$  (km/mol).

$i$	$\mu_{ix}$	$\mu_{iy}$	$\mu_{iz}$		
1	0.0000	-0.0326	-0.0350		
2	-0.0311	-0.0093	0.0323		
3	-0.0185	0.0275	-0.0150		
4	0.0185	0.0275	-0.0150		
5	0.0311	-0.0093	0.0323		
$j$	1	2	3	4	5
$E_j$	1487.3	1492.8	1497.5	1499.1	1524.2
$I_j$	0.25	4.76	3.67	4.81	0.18

<sup>a</sup>Elements have dimensions  $(\text{km/mol})^{1/2}/\text{cm}^{-1}$ . See text and Eq. (15) for details.

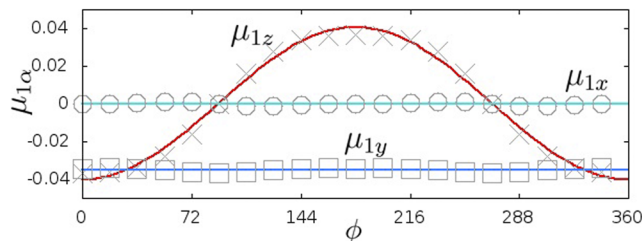


**FIG. 3.** The linear dipole matrix elements for the scissor mode 1 as a function of the pseudorotation angle  $\phi$ . Points correspond to conformers in Fig. 2. The lines correspond to linear least squares fits. Matrix elements are scaled to have units  $\sqrt{\text{km/mol/cm}^{-1}}$ ; see text following Eq. (15) for details.

The  $\phi$  dependencies of the remaining dipoles are determined by tracking the equivalencies of environments as a function of  $\phi$  and the orientation of  $\text{CH}_2$  groups as one moves around the cyclopentane ring. We find

$$\begin{aligned} \mu_{xk} &= d_{y0} \sin[2(k-1)\pi/5], \\ \mu_{yk} &= d_{y0} \cos[2(k-1)\pi/5], \\ \mu_{zk} &= (-1)^{k-1} d_{z1} \cos[\phi - (k-1)\pi/5]. \end{aligned} \quad (17)$$

These matrix elements take on a simpler form using the definition of  $f_k$  in Eq. (6) and using the dipole operators  $\mu_\pm = (\mu_y \pm i\mu_x)/\sqrt{2}$ . We find

$$\begin{aligned} \mu_{\pm,k} &= 2^{-1/2} d_{y0} f_k^{\pm 2} \\ \mu_{z,k} &= (-1)^{k-1} d_{z1} [e^{i\phi} f_k^* + e^{-i\phi} f_k]/2. \end{aligned} \quad (18)$$

The corresponding elements in the symmetric basis of Eq. (8) are evaluated using the identities

$$\sum_{k=1}^5 [U_{\ell_v,k}]^* f_k^{2j} = \sqrt{5} \delta_{\ell_v,j}, \quad (19)$$

$$\sum_{k=1}^5 (-1)^{k-1} [U_{\ell_v,k}]^* f_k^{\pm 1} = \sqrt{5} \delta_{\ell_v,\mp 2}. \quad (20)$$

The nonzero elements are

$$\begin{aligned} \langle \psi_{\pm 1} | \mu_{\mp} | \psi_{\text{gs}} \rangle &= (5/2)^{1/2} d_{y0}, \\ \langle \psi_{\pm 2} | \mu_z | \psi_{\text{gs}} \rangle &= (5/4)^{1/2} d_{z1} e^{\pm i\phi}. \end{aligned} \quad (21)$$

This result is consistent with previous works<sup>3,17</sup> describing the scissor fundamentals in which the  $z$  component of the dipole leads to  $\Delta\ell = \pm 1$  transitions.

## V. CH STRETCHES

Our modeling of the CH stretches follows that of the  $\text{CH}_2$  scissor modes. We begin by constructing the  $10 \times 10$  localized CH

stretch Hamiltonian matrices of the  $b_1^+$  and  $t_1^+$  structures. We next determine the  $\phi$ -dependent elements of a more general  $10 \times 10$  matrix  $\mathbf{H}$  by tracking equivalencies as a function of pseudorotation. The resulting Hamiltonian is symmetrized and expressed in a form that allows for straightforward evaluation of matrix elements in a direct product basis set of CH stretches and pseudorotation degrees of freedom. As a last step, we describe the form of the dipole moments.

### A. CH stretch Hamiltonian matrix

To keep track of the equivalent environments, we number the H atoms 1–10 in a clockwise fashion, as shown in Fig. 1. The  $\phi = 0$  geometry of this molecule is shown at the left in Fig. 1. The local mode CH stretch Hamiltonian matrix of the  $b_1^+$  structure is written as  $\mathbf{H}$  evaluated at  $\phi = 0$ . For this structure, the local stretch frequencies of CH<sub>1</sub> and CH<sub>2</sub> are 3062.4 and 3021.4 cm<sup>-1</sup>, respectively, at the DFT level we have used throughout. The two environments are reminiscent of the equatorial and axial geometries of cyclohexane, with the equatorial corresponding to the higher frequency vibration.

Tracking the  $\phi$  dependence of the matrix element follows the same consideration as the scissor modes. From Fig. 2, we see that a local scissor frequency is the same at  $\phi = 0$  and  $\pi$ . In contrast, the two CH stretch environments are switched for the  $b_1^-$  structure. As a result,  $H_{1,1}(\phi = \pi) = 3021.4$  cm<sup>-1</sup>. To maintain equations similar to those for the scissors, it is convenient to introduce an array that tracks the equivalent CH stretches with successive pseudorotation

$$\mathbf{b} = \{1, 4, 5, 8, 9, 2, 3, 6, 7, 10\}. \quad (22)$$

The use of this array is not needed for the scissors, since after a rotation of  $\phi = \pi$  one has completed a cycle of the five scissor modes. In contrast, for the stretches for  $\phi = \pi$ , hydrogen H<sub>2</sub> is in an equivalent environment to that of H<sub>1</sub> at  $\phi = 0$ . The use of this array leads to

$$H_{b_k, b_{k'}}(\phi) = \frac{1}{2} \sum_{n=0}^2 s_{j,n} \left[ e^{in\phi} f_k^{-n/2} f_{k'}^{-n/2} + c.c. \right], \quad (23)$$

where  $j = |k' - k|$ . This result has the same form as the scissor Hamiltonian of Eq. (5). The fit coefficients  $s_{j,n}$  are shown in Table III. The points correspond to matrix elements of the “bent” and “twist” geometries, and the fit is shown as a solid line (see Fig. 4). The large difference in the diagonal matrix elements ( $n = 1$ ) at  $\phi = 0$  and  $\pi$  is due to the above-mentioned switch between axial and equatorial geometries.

The stretch Hamiltonian takes a simpler form in a  $D_{5h}$  symmetrized basis. We transform to this basis using the complex representation

$$\psi_{\ell_v}^{(s/a)} = \sum_{k=1}^{10} U_{\ell_v, k}^{s/a} \chi_k, \quad (24)$$

where the  $\chi_k$  are the local stretch basis functions. The matrix elements are

$$U_{\ell_v, b_k}^{s/a} = (\sigma_{s/a})^{k-1} f_k^{2\ell_v} / \sqrt{10}, \quad (25)$$

where  $\sigma_{s/a} = \pm 1$ . The  $\pm$  is for the linear combinations of the symmetric and asymmetric CH<sub>2</sub> stretches, respectively, on each of the

**TABLE III.** Expansion coefficients  $s_{j,n}$  for the CH stretch Hamiltonian in wavenumbers (cm<sup>-1</sup>) [see Eq. (23)].

$j$	$s_{j,0}$	$s_{j,1}$	$s_{j,2}$
0	3049.356 79	21.345 33	-8.029 96
1	-3.052 51	6.066 20	-0.029 90
2	1.136 04	-0.403 87	0.413 72
3	0.472 83	0.558 75	0.033 10
4	7.295 93	-0.474 54	1.762 96
5	-16.275 46	-0.000 00	1.172 09
6	7.295 93	0.474 54	1.762 96
7	0.472 83	-0.558 75	0.033 10
8	1.136 04	0.403 87	0.413 72
9	-3.052 51	-6.066 20	-0.029 90

five carbon atoms. As was the case for the scissor modes, the  $\ell_v$  values run from -2 to 2. For the symmetric states the  $\pm \ell_v$  pairs have  $e_{\ell_v}^{\prime}$  symmetry, and the  $\ell_v = 0$  states have  $a_1^{\prime}$  symmetry. For the asymmetric states the  $\pm \ell_v$  pairs have  $e_{\ell_v}^{\prime\prime}$  symmetry and the  $\ell_v = 0$  states have  $a_2^{\prime\prime}$  symmetry.

Transforming the Hamiltonian of Eq. (23) to the symmetrized Hamiltonian, analogous to that of the scissor Hamiltonian of Eq. (10), leads to

$$\mathcal{H}^{s,s} = \begin{pmatrix} 3027 & -4c_2 & 0 & 0 & -2c_2^* \\ -4c_2^* & 3033 & -6c_2 & 0 & 0 \\ 0 & -6c_2^* & 3045 & -6c_2 & 0 \\ 0 & 0 & -6c_2^* & 3033 & -4c_2 \\ -2c_2 & 0 & 0 & -4c_2^* & 3027 \end{pmatrix}, \quad (26)$$

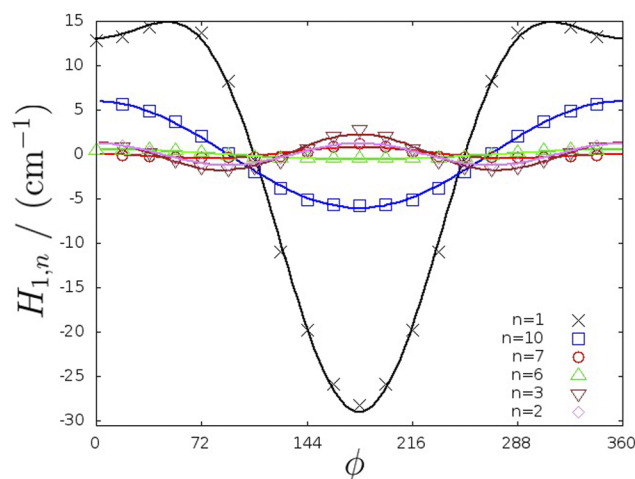


**FIG. 4.** Plot of the deviations of the  $H_{1,n}$  matrix elements from the average values plotted as a function of the pseudorotation angle. The  $\phi = 0$  structure is shown at the left of Fig. 1. The order of the  $n$  values follows the element of the array  $\mathbf{b}$  in Eq. (22). The least squares fit, whose results are reported in Table III, takes the form of Eq. (23).

$$\mathcal{H}^{a,a} = \begin{pmatrix} 3049 & -3c_2 & 0 & 0 & -1c_2^* \\ -3c_2^* & 3071 & -5c_2 & 0 & 0 \\ 0 & -5c_2^* & 3088 & -5c_2 & 0 \\ 0 & 0 & -5c_2^* & 3071 & -3c_2 \\ -1c_2 & 0 & 0 & -3c_2^* & 3049 \end{pmatrix}, \quad (27)$$

$$\mathcal{H}^{s,a} = \begin{pmatrix} 0 & 0 & 4c_1^* & 8c_1 & 0 \\ -1c_3 & 0 & 0 & 10c_1^* & 14c_1 \\ 16c_1 & 0 & 0 & 0 & 16c_1^* \\ 14c_1^* & 10c_1 & 0 & 0 & -1c_3^* \\ 0 & 8c_1^* & 4c_1 & 0 & 0 \end{pmatrix}. \quad (28)$$

These matrices are reported with additional significant figures in the [supplementary material](#).

The stretch Hamiltonian, when combined with the particle in a ring states of the pseudorotation degree of freedom, leads to matrix elements of the same form as those for the scissors given in Eq. (12). All diagonal terms are subsequently scaled by 0.9609. This value has been increased from the 0.960 value used in our localized model of CH stretches<sup>12</sup> to better match with the experimental results for the most intense high energy feature of the spectrum.

## B. CH stretch dipoles

The dipole matrix elements  $\mu_{1\alpha}$  for CH<sub>1</sub> are shown in Fig. 4 as a function of  $\phi$ . Also shown are the results of the least squares fits,

$$\begin{aligned} \mu_{1x} &= \sum_{n=1}^2 d_n^{(x)} \sin(n\phi), \\ \mu_{1y} &= \sum_{n=0}^2 d_n^{(y)} \cos(n\phi), \\ \mu_{1z} &= \sum_{n=0}^2 d_n^{(z)} \cos(n\phi), \end{aligned} \quad (29)$$

for each of the components. The coefficients are given in Table IV.

The  $\phi$  dependence of the dipole matrix elements of the remaining CH stretches is determined as it was for the scissor modes, and details are included in the [supplementary material](#). Combining a symmetrized representation with the dipole matrix elements

$$\mu_k^\pm = [\mu_{ky} \pm i\mu_{kx}]/\sqrt{2} \quad (30)$$

leads to the results of Table V. The selection rules are relatively simple. Both DFT and MP2 levels of theory are reported. The ratios of the two most intense transitions are similar for the two levels of theory, with the DFT ratio value of 1.33 being slightly larger than the 1.19 MP2 ratio.

In contrast to the scissor modes, the perpendicular transitions have  $\ell = 0$ . Here, there are additional  $\Delta\ell = \pm 1, \pm 2$  vibrational transitions. The full stretch/pseudorotation symmetry leads to the result that only  $\Delta\ell_t = \pm 2$  perpendicular transitions are allowed. We will return to a more detailed discussion of these results in Sec. VI.

TABLE IV. Dipole expansion coefficients<sup>a</sup> for Eq. (29).

$\alpha$	$d_0^{(\alpha)}$	$d_1^{(\alpha)}$	$d_2^{(\alpha)}$
$x$		0.008 34	-0.005 76
$y$	-0.080 13	-0.044 04	0.007 22
$z$	0.065 36	-0.047 23	-0.001 26

<sup>a</sup>Dimensions are (km/mol)<sup>1/2</sup>/cm<sup>-1</sup>.

## C. Overtones and combination bands

The correct description of the CH stretch fundamentals requires the inclusion of the overtones and combination states of the scissor modes due to their near degeneracy with the stretches and the large Fermi coupling coefficients. Since we know the diagonal and off-diagonal elements of the  $5 \times 5$  matrix describing a single quantum of excitation, we can follow the properties of harmonic oscillators and their matrix elements and generate the  $15 \times 15$  local mode Hamiltonian matrix.

In order to exploit symmetry, we divide these 15 states into three groups. The first group includes the states with single excitation on neighboring groups. These five states

$$|1, 1, 0, 0, 0\rangle, |0, 1, 1, 0, 0\rangle, \dots, |1, 0, 0, 0, 1\rangle \quad (31)$$

are written as  $|\chi_k^{(1)}\rangle$  with  $k = 1-5$ . The second set of states

$$|1, 0, 1, 0, 0\rangle, |0, 1, 0, 1, 0\rangle, \dots, |0, 1, 0, 0, 1\rangle \quad (32)$$

are written as  $|\chi_k^{(2)}\rangle$  with  $k = 1-5$ . The final set are the five overtones  $|\chi_k^{(3)}\rangle$ , which are

$$|2, 0, 0, 0, 0\rangle, |0, 2, 0, 0, 0\rangle, \dots, |0, 0, 0, 0, 2\rangle. \quad (33)$$

These 15 basis functions lead to a scissor matrix consisting of nine  $5 \times 5$  sub-matrices  $\mathbf{H}^{m,m'}$ . Here, the superscripts correspond to the three different types of doubly excited states.

The  $\phi$  dependence of the symmetrized Hamiltonians is determined numerically. At various angles  $\phi$ , we construct the local mode Hamiltonian and transform to the symmetrized representation. We find that the symmetrized Hamiltonians  $\mathcal{H}_{\ell_v, \ell_v'}^{m, m'}$  all have the same  $\phi$  dependence as the one quantum states of Eq. (10).

TABLE V. Nonzero CH stretch dipole matrix elements<sup>a</sup> written as a product  $fg$ .

Element	$f^b$	$f^c$	$g$
$\langle \Psi_0^a   \mu_z   \Psi_{gs} \rangle$	0.2067	0.1642	1
$\langle \Psi_{\pm 2}^s   \mu_z   \Psi_{gs} \rangle$	-0.0747	-0.0666	$e^{\pm i\phi}$
$\langle \Psi_{-1}^s   \mu_+   \Psi_{gs} \rangle$	-0.1792	0.1504	1
$\langle \Psi_{-2}^a   \mu_+   \Psi_{gs} \rangle$	-0.0586	-0.0521	$e^{i\phi}$
$\langle \Psi_{-1}^a   \mu_+   \Psi_{gs} \rangle$	-0.0399	-0.0347	$e^{-i\phi}$
$\langle \Psi_0^s   \mu_+   \Psi_{gs} \rangle$	0.0145	0.0138	$e^{2i\phi}$
$\langle \Psi_2^s   \mu_+   \Psi_{gs} \rangle$	0.0016	0.0018	$e^{-2i\phi}$

<sup>a</sup>Dimensions are (km/mol)<sup>1/2</sup>/cm<sup>-1</sup>.

<sup>b</sup>B3LYP/6-311++(d,p).

<sup>c</sup>MP2/cc-pVTZ.

The transformation to symmetrized basis for the overtones is that same as that for the fundamentals [see Eq. (8)]. However, the combination bands require a phase shift

$$U_{\ell_v, k}^m = \exp[i(\ell_v(k-1) + \delta)\phi_5]/\sqrt{5}, \quad (34)$$

where  $\delta = 0.5$  and  $1.0$  for the  $m = 1$  and  $2$   $|\chi_k^{(m)}\rangle$  states, respectively. The  $\mathcal{H}^{m, m'}$  matrices are provided in the [supplementary material](#). The symmetrized basis states are denoted  $|\psi_{\ell_v}^{(m)}\rangle$ , where the  $m = 1-3$  denotes the group and serves to distinguish them from the stretch states that have the same form but are labeled with a  $(s/a)$  superscript.

The overtones are coupled to the CH fundamentals via Fermi coupling. In a previous work, the matrix element describing the coupling between a CH local mode and a contiguous local CH<sub>2</sub> scissor overtone was found to take a value of  $V_F \approx 22 \text{ cm}^{-1}$ .<sup>12</sup> That value is used here. In the symmetrized representation used herein, only the symmetric CH stretches are coupled and the coupling elements are

$$\langle \psi_{\ell_v}^{(s)} | V | \psi_{\ell_v'}^{(3)} \rangle = \sqrt{2} V_F \delta_{\ell_v, \ell_v'} \quad (35)$$

#### D. Symmetry

In [Table VI](#), we provide symmetry labels for direct product basis functions  $|\ell_v^{(s/a)}, \ell\rangle$ . The symmetry of both the CH<sub>2</sub> scissor states and the symmetric CH stretch states are determined by their values of  $\ell_v$ , so the scissor states are not included in our discussion of symmetry. The coupling connectivity allows one to determine the symmetry of any state based on the states that are included. As noted above, the  $\ell_t$  value determines the symmetry label subscript. The a states have  $\ell_t = 0$ , otherwise the state is doubly degenerate. The prime and double primed states are distinguished by the  $\sigma_h$  reflection symmetry. The degenerate states  $|\ell_v^a, \ell\rangle$  have prime or double prime symmetry depending on whether  $\ell$  is odd or even, respectively. States  $|\ell_v^s, \ell\rangle$  have prime or double prime symmetry depending on whether  $\ell$  is even or odd, respectively. The symmetries  $a_2'$  and  $a_1''$  are distinguished by the  $C_2$  operation. Under this operation,  $\sin(5\phi)$  goes to  $-\sin(5\phi)$ ,  $\psi_0^s$  goes to  $\psi_0^s$ , and  $\psi_0^a$  goes to  $-\psi_0^a$ ; consequently, we can designate the states as shown in [Table VI](#).

**TABLE VI.** Symmetry designation of the vibration/pseudorotation basis.

$\ell_t$	Symmetry	State 1	State 2
0	$a_1'$	$\psi_0^s$	$\psi_2^a e^{i\phi} + \psi_{-2}^a e^{-i\phi}$
0	$a_2''$	$\psi_0^a$	$\psi_2^s e^{i\phi} + \psi_{-2}^s e^{-i\phi}$
0	$a_2'$	$\psi_0^s \sin(5\phi)$	$\psi_2^s e^{i\phi} - \psi_{-2}^s e^{-i\phi}$
0	$a_1''$	$\psi_0^a \sin(5\phi)$	$\psi_2^a e^{i\phi} - \psi_{-2}^a e^{-i\phi}$
1,4	$e_2''$	$\psi_0^s e^{i\phi}$	$\psi_0^s e^{-i\phi}$
1,4	$e_2'$	$\psi_0^a e^{i\phi}$	$\psi_0^a e^{-i\phi}$
2,3	$e_1'$	$\psi_0^s e^{2i\phi}$	$\psi_0^s e^{-2i\phi}$
2,3	$e_1''$	$\psi_0^a e^{2i\phi}$	$\psi_0^a e^{-2i\phi}$

## VI. RESULTS

We first present results for the scissor fundamentals and then the CH stretches. We calculate spectra with and without rotations included. We include the rotational contribution for each vibrational transition by replacing the line with a rotational line shape. These line shapes, shown in [Fig. 5](#), are obtained for parallel and perpendicular transitions of an oblate symmetric top in which we use the average of the  $A$  and  $B$  rotational constants reported in [Table VII](#). We assume a Boltzmann distribution of pseudorotation states with a temperature of  $-26.1^\circ\text{C}$  for the CH<sub>2</sub> scissor fundamentals and  $T = -50.0^\circ\text{C}$  for the CH stretch fundamentals, and these values corresponding to the temperature of the experiments. All other vibrational modes are assumed to be unpopulated.

Our spectral results for the scissor fundamentals are reported in [Fig. 6](#). For all these spectra, we have scaled the scissor frequencies by 0.975. This scaling was determined empirically in earlier works.<sup>12,21</sup> The top panel shows results for which the symmetrized scissor modes are decoupled from the pseudorotation by setting the off-diagonal terms in Eq. (11) to zero. The resulting spectrum follows from [Fig. 3](#) where the angular dependence of the scissor dipole is shown. The lack of  $\phi$  dependence for the perpendicular dipole matrix element leads to  $\Delta\ell = 0$  vibrational transitions, as is evident from Eq. (21). This property of the dipole in turn leads to a large intensity buildup of  $7.8 \text{ km/mol}$  due to the overlapping perpendicular transitions at  $1460.1 \text{ cm}^{-1}$ . This wavenumber value is the scaled value of the  $1497.6 \text{ cm}^{-1}$  matrix elements associated with the  $\psi_{\pm 1}$  symmetrized scissor states of Eq. (11). The intensity is similar to the Gaussian intensity of  $9.3 \text{ km/mol}$  for the  $e_1'$  CH<sub>2</sub> scissor normal mode, obtained at an energy minimized structure constrained to have  $D_{5h}$  symmetry with the B3LYP/6-311++(d,p) level of theory.<sup>28</sup> We use the previously determined  $B_\phi = 2.8 \text{ cm}^{-1}$  value<sup>7</sup> for the ground and excited scissor states. This value is

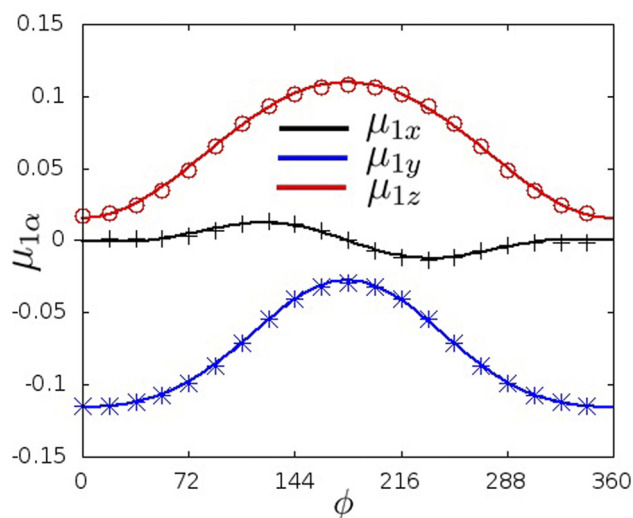


**FIG. 5.** Plot of components of the CH<sub>1</sub> stretch dipole matrix elements  $\langle 0 | \mu_\alpha | \chi_1 \rangle$  as a function of the pseudorotation angle  $\phi$ . The fit lines are given in Eq. (29). Matrix elements are scaled to have units  $\sqrt{\text{km/mol/cm}^{-1}}$ ; see text following Eq. (15) for details.

**TABLE VII.** Rotational constants (GHz) obtained from B3LYP/6-311++(d,p) level calculation of the  $b_1^+$  structure.

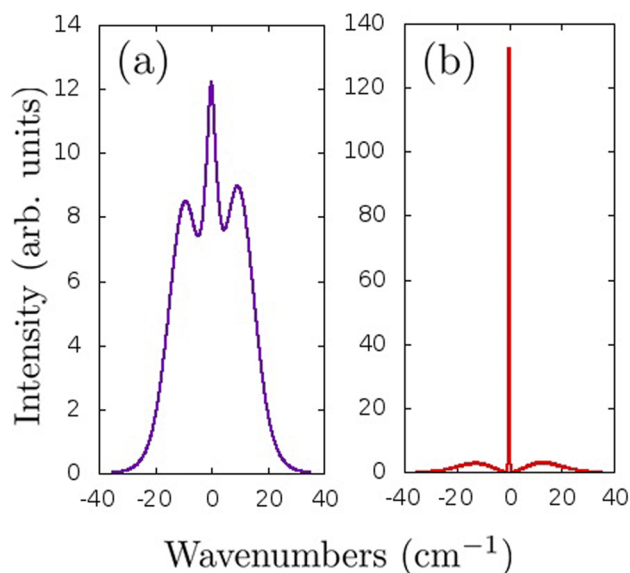
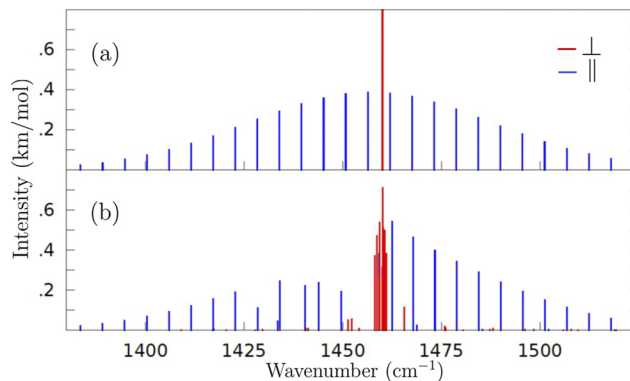
A	B <sup>a</sup>	C
6.466 82	6.465 37	3.726 16

<sup>a</sup>The experimental value is  $B = 6.484\,93$  GHz.<sup>7</sup>

important for the parallel vibrational transitions. These transitions are dominated by  $\Delta\ell = \pm 1$  transitions that result from the cosine behavior of the scissor dipole matrix elements observed in Fig. 3. These transitions are centered at  $1453.8\text{ cm}^{-1}$ , a value that follows from the scaled  $1491.1\text{ cm}^{-1}$  matrix elements associated with the  $\psi_{\pm 2}$  symmetrized scissor states of Eq. (11).

In Fig. 6(b), we show model results for the scissor/pseudorotation contributions to the Hamiltonian. The similarity in structure of panels (a) and (b) is due to the small size of the off-diagonal couplings in Eq. (11). The most profound effects are found for the small  $\ell$  states at the center of the spectra. Here, the sizes of the off-diagonal elements in Eq. (11) are comparable to the spacings between the pseudorotation levels so that resonant couplings are present. For the larger  $\ell$  states, the spacings between the pseudorotation levels increase and the coupled states are no longer nearly resonant.

The theoretical spectrum of Fig. 7 is the result of convoluting each of the vibrational transitions of Fig. 6(b) with the appropriate rotational vibrational profile of Fig. 5. One sees that any structure in the perpendicular vibrational transitions is lost due to the large width of the rotational vibrational profile. In contrast, the parallel vibrational transitions are characterized by sharp Q-branch transitions. Also shown in Fig. 7 are the experimental results. One

**FIG. 6.** Rotational vibrational profiles (a) perpendicular and (b) parallel transitions of an oblate symmetric top with rotational constants of Table VII. The Q-branch transitions in (b) owe their intensities to many overlapping transitions. Individual lines are broadened by Gaussians  $\exp[-(l - l_0)/\sigma^2]$  with  $\sigma = 0.25\text{ cm}^{-1}$ .**FIG. 7.** Theoretical impulse plot spectra for  $\text{CH}_2$  scissor fundamentals comparing the pure vibrational spectrum with (a) no coupling and (b) coupling to the pseudorotation degree of freedom. The perpendicular transition in (a) at  $1460.1\text{ cm}^{-1}$  has an intensity of  $7.8\text{ km/mol}$ . The temperature is  $-26.1^\circ\text{C}$ .

can see that our theory captures the main spectral features including the ones near the center that are due to scissor/pseudorotation couplings.

The model predicts that, for larger values of  $\ell$ , there is little coupling between the scissors and the pseudorotation degrees of freedom. As a result, it predicts a sequence of evenly spaced lines with a spacing of approximately  $2B_\phi$  [see Eq. (2)] as described previously in the work of Bauman and Laane.<sup>3</sup> In contrast, if we look more closely at the wings of the experimental spectrum that corresponds to transitions to larger  $|\ell|$  values shown Fig. 8, we see that there is substantial fractionation of the lines even beyond that which was observed by Bauman and Laane.<sup>3</sup> Our work does not address the origins of the mixing, but those authors speculated that Coriolis coupling maybe responsible for the observed state mixing. A low-resolution experimental spectrum is provided to highlight the underlying pattern of equally spaced transitions as well as the extensive state mixing observed at the high-spectral resolution of the experiment. The best our model can do is capture these low-resolution features as shown by the impulses in this figure. Table VIII compares the experimental and theoretical results. The nondegenerate states are those for which  $l_i = 0$ . All states in the table correspond to excitation of the  $\psi_2$  scissor state except where noted.

In contrast to the scissor spectrum, in which the parallel transitions are to a good approximation  $\Delta\ell = \pm 1$  and the perpendicular transitions  $\Delta\ell = 0$ , the CH stretch excitation is predominantly  $\Delta\ell = 0$  transitions for both the symmetric and asymmetric stretches. This feature is evident in the dipole matrix elements reported in Table V where the two leading terms have no  $\phi$  dependence and correspond to excitation of the stretch states  $\psi_0^a$  and  $\psi_{\pm 1}^z$ . The former is a parallel transition (observed near  $2966\text{ cm}^{-1}$ ), and the latter a perpendicular transition (observed near  $2880\text{ cm}^{-1}$ ). These states have  $a_2''$  and  $e_1'$  symmetries, respectively. The transitions are the expected allowed transitions for a molecule with  $D_{5h}$  symmetry.

To highlight the role of the dipole selection rules, in Figs. 9(a) and 9(b), we show a spectrum for the CH stretch Hamiltonian for which we have decoupled the stretches from the pseudorotation by setting the off-diagonal terms to zero in Eqs. (26)–(28). We also turn

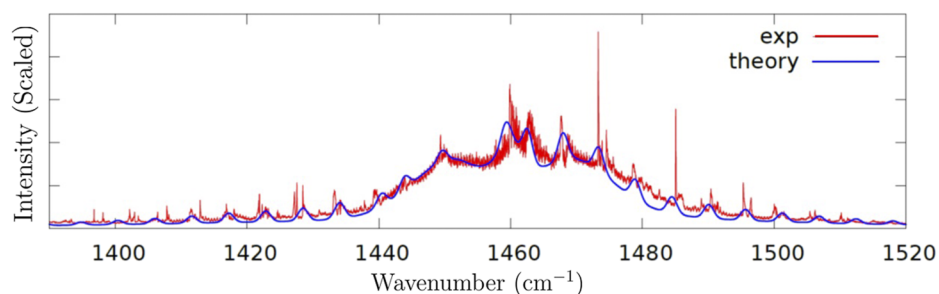


**FIG. 8.** Comparison of experiment and theory. The temperature is  $-26.1^{\circ}\text{C}$ . Theoretical intensities are scaled to match experiment. Individual lines are broadened by Gaussian functions  $\exp[-(l-l_0)/\sigma^2]$  with  $\sigma = 0.25\text{ cm}^{-1}$ .

off the Fermi coupling to the scissor overtones. In this limit, the symmetric and antisymmetric manifolds of states are decoupled, and we can consider the spectral contributions of these states in (a) and (b), respectively.

Focusing on just the transitions to the symmetric stretch manifold of states shown in Fig. 9(a), one finds a spectrum similar

**TABLE VIII.** Comparison of the most intense experimental (low-resolution) and theoretical scissor transition energies ( $\text{cm}^{-1}$ ) for the parallel transitions.

Expt.	Model	Intensity	E (upper)	$\ell'$	$\ell$
1384.7	1383.6	0.022	1856.8	13	12
1392.4	1389.2	0.033	1792.4	12	11
1397.8	1394.8	0.048	1733.6	11	10
1402.6	1400.4	0.068	1680.4	10	9
1407.7	1406.0	0.093	1632.8	9	8
1412.0	1411.6	0.122	1590.8	8	7
1417.1	1417.2	0.154	1554.4	7	6
1422.4	1422.8	0.188	1523.6	6	5
1428.4	1428.47	0.110	1498.5	5	4 <sup>a</sup>
	1428.53	0.109	1498.5	5	4 <sup>b</sup>
1433.5	1433.5	0.045	1458.7	3	0 <sup>c</sup>
	1434.1	0.244	1478.9	4	3
	1440.4	0.222	1465.6	3	2
	1443.9	0.238	1455.1	2	1
1449.9	1449.6	0.192	1452.4	1	0
1460.4	1459.3	0.382	1459.3	0	1 <sup>d</sup>
1462.8	1462.6	0.542	1465.4	1	2
1468.8	1467.9	0.463	1479.1	2	3
1473.4	1473.4	0.398	1498.6	3	4
1478.4	1478.9	0.343	1523.7	4	5
1485.2	1484.5	0.290	1554.5	5	6
1490.4	1490.1	0.239	1590.9	6	7
1495.6	1495.7	0.192	1632.9	7	8
1500.3	1501.3	0.149	1680.5	8	9
1505.8	1506.9	0.113	1733.7	9	10
1510.3	1512.4	0.082	1792.4	10	11
1515.2	1518.0	0.058	1856.8	11	12
1521.0	1523.6	0.040	1926.8	12	13
1525.5	1529.2	0.026	2002.4	13	14

<sup>a</sup>Leading description is  $|2, -4\rangle - |-2, 4\rangle$ .

<sup>b</sup>Leading description is  $|2, -4\rangle + |-2, 4\rangle$ .

<sup>c</sup>Leading description is  $0.9|1, 0\rangle + 0.4|2, -2\rangle$ .

<sup>d</sup>Leading description is  $|2, 1\rangle + |-2, -1\rangle$ .

to that of the uncoupled scissor spectrum of Fig. 7(a). This similarity is partly due to the same dipole selection rules. The intense peak at  $2913\text{ cm}^{-1}$  is due to  $\Delta\ell = 0$  perpendicular transitions to the  $\psi_{\pm 1}^s$  manifold of states. One each side of this peak, we see a series of evenly spaced parallel transitions due to the  $\Delta\ell = \pm 1$  selection rule. These transitions correspond to excitation of the  $\psi_{\pm 2}^s$  manifold of states. There is, however, an additional reason for the similarity. Both sets of the  $\ell_v = \pm 1$  states are about  $6\text{ cm}^{-1}$  higher in energy than their  $\ell_v = \pm 2$  counterparts. This similarity can be seen by comparing the Hamiltonians of Eqs. (11) and (26).

The spectral transitions to the asymmetric CH stretches, shown in Fig. 9(b), result from the allowed vibrational transitions to states  $\psi_{\ell_v}^a$  with  $\ell_v = 0, \pm 1$ , and  $\pm 2$ . The relative intensities follow from the

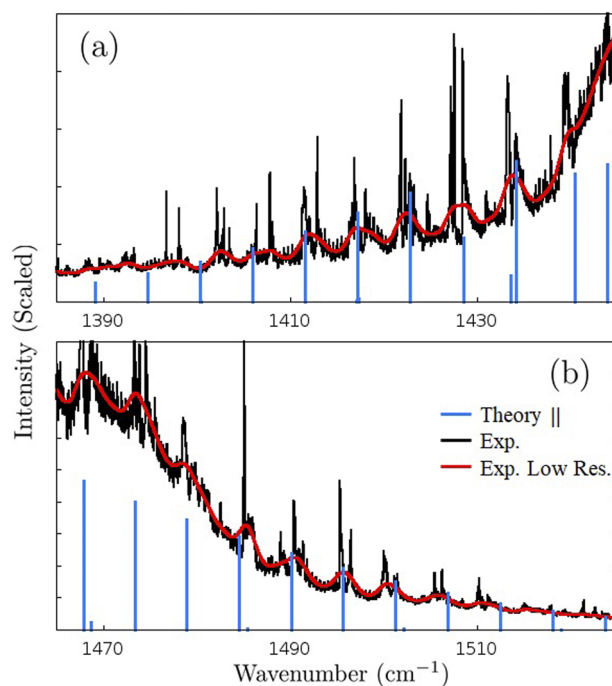


**FIG. 9.** High-resolution experimental spectrum showing the wings of the spectral region associated with (a)  $\Delta\ell = -1$  and (b)  $\Delta\ell = +1$  transitions of the scissor fundamental. Theoretical rotationless spectrum for the parallel transitions shown as impulses is compared to a low-resolution spectrum obtained by convoluting the experimental spectrum with a Gaussian line shape with  $\sigma = 1.0\text{ cm}^{-1}$ .

results of Table V. The latter set of states lie lower in energy than the  $\ell_v = 0$  state, leading to a perpendicular  $\Delta\ell = \pm 1$  set of transitions that are predominantly shifted to lower energies than the most intense  $\Delta\ell = 0$  parallel feature.

When we allow the CH stretches to couple to the pseudorotational degree of freedom, a qualitatively different spectrum emerges as seen in Fig. 9(c). The reason for the dramatic coupling is apparent in the form of Eqs. (26)–(28). The leading coupling terms between the stretches are those terms proportional to  $e^{\pm i\phi}$  found in the coupling between the symmetric and antisymmetric stretches  $\mathcal{H}^{s,a}$ . As an example, consider the term proportional to  $14e^{-i\phi} \text{ cm}^{-1}$ . This term couples the bright state  $\psi_1^s$  to the  $\psi_{-2}^a$  state. The difference in the vibrational contribution to the energies of these two states is just  $16 \text{ cm}^{-1}$ . This and other couplings lead to substantial state mixing as revealed by the differences between Figs. 9(a)–9(c). Not all states, however, are strongly mixed. The bright state  $\psi_0^a$  is energetically removed from the other CH stretch states. Its unscaled (scaled) energy is  $3088$  ( $2967$ )  $\text{cm}^{-1}$ . This state is directly coupled to the degenerate  $\psi_{\pm 2}^s$  states whose unscaled (scaled) energies are  $3027$  ( $2909$ )  $\text{cm}^{-1}$ . Since this energy difference is large compared to the coupling matrix of  $4e^{\pm i\phi} \text{ cm}^{-1}$ , we expect and find that the  $\psi_0^a$  manifold of states are relatively uncoupled from the other stretching states.

Any coupling that is present at these higher transition energies is typically indirect coupling. For example, in the absence of the Fermi coupling, the  $|0^a, 2\rangle$  state is coupled to the state  $|-1^a, 4\rangle$ , which in turn is coupled to  $|1^s, 5\rangle$  as described by the Hamiltonian matrix

$$\mathbf{H}_c = \begin{pmatrix} 2978 & -5 & 0 \\ -5 & 2996 & 10 \\ 0 & 10 & 2984 \end{pmatrix}. \quad (36)$$

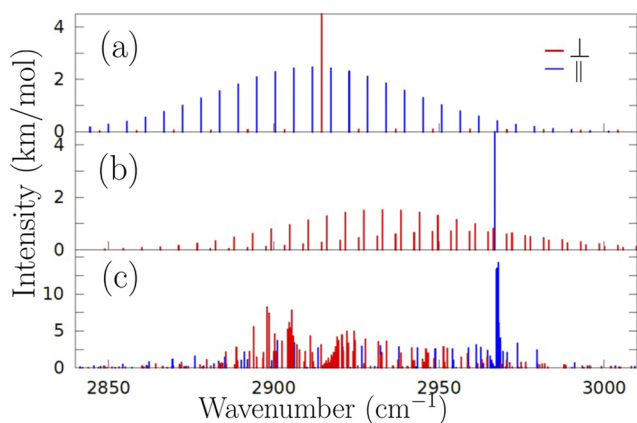


**FIG. 10.** Impulse plots of CH stretch vibrational spectra with no coupling to pseudorotation for (a) symmetric and (b) antisymmetric CH stretches. Peaks in (a) at  $2913 \text{ cm}^{-1}$  and (b) at  $2965 \text{ cm}^{-1}$  have intensities of  $187$  and  $126 \text{ km/mol}$ , respectively. (c) Impulse plot resulting from the coupling of CH stretches to pseudorotation degree of freedom. Model assumes no Fermi coupling to scissor modes. The temperature is set at  $-50.0 \text{ }^\circ\text{C}$ .

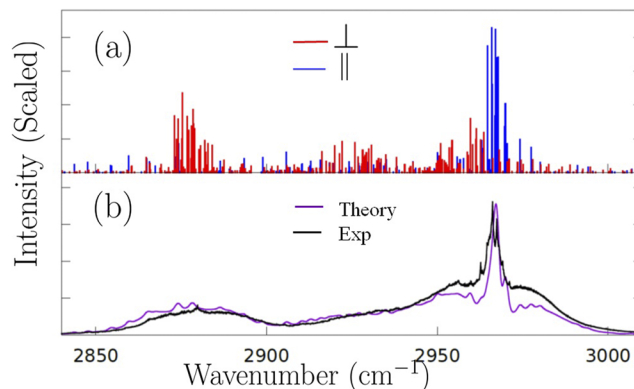


**FIG. 11.** Comparison of experiment and theory with Fermi coupling to the scissor modes. (a) Impulse plot of spectrum resulting from CH stretches and scissors coupled to the pseudorotation degree of freedom. (b) Comparison of theory with rotations and experiment in which  $T = -50 \text{ }^\circ\text{C}$ ; the theoretical intensities are scaled and individual lines are broadened by Gaussian functions  $\exp[-(I - I_0)/\sigma^2]$  with  $\sigma = 0.5 \text{ cm}^{-1}$ .

Here, we are using the notation  $|\ell_v^{s/a}, \ell\rangle$  to describe the direct product basis functions.

In order to compare to experiment one needs to include the Fermi coupling to the scissor modes. We include these interactions in our results of Fig. 10(a). Comparing this figure to Fig. 9(c) allows one to see the extent to which the Fermi coupling affects the spectral features. When one includes the rotational vibrational profiles, as was done for the scissor fundamental, we obtain the results of Fig. 10(b), one can see the extent of the agreement between our model and the experimental spectrum. Our model fails to capture the detailed features. Given its simplicity, its reliance on DFT scaled calculations, its assumption of transferability of anharmonic coupling terms, and its neglect of most of the degrees of freedom, we consider the comparison to be good.

One of the most striking features of the CH stretch spectrum is the absence of the clearly evident  $\Delta\ell = \pm 1$  progressions observed in the  $\text{CH}_2$  scissor fundamental. In the context of our model, these lines are absent due to the large variations of the CH stretch site energies in our local mode model (see Fig. 11) as the CH stretch moves between equatorial and axial like environments over the course of pseudorotation. These variations lead to the large coupling terms found in  $\mathcal{H}^{s,a}$  of Eq. (28) and the subsequent state-mixing predicted by our model and as evidenced by the dramatic difference between the panels of Figs. 9(a)–9(c).

## VII. CONCLUSIONS

In this paper, we report recently measured IR spectra for the  $\text{CH}_2$  scissor vibrations and CH stretch vibrations of cyclopentane and develop models that describe these vibrations and how they are affected by pseudorotation. This work extends previous studies of this molecule by explicitly including the potential terms, calculated with electronic structure methods, that couple these modes as

a function of pseudorotation. This work builds on our previous local mode treatments of these vibrations. The resulting spectral predictions of that model, which had been shown to be successful for both open and close shell systems as well as ground and excited states, are shown to qualitatively describe many of the spectral features of cyclopentane.

The distinguishing feature of this work is the combination of local modes and symmetry considerations that lead to simple direct product matrix representations that form the basis of our spectral calculations. In the case of the scissor vibrations, the coupling between the scissor vibrations modifies the uncoupled spectrum with intriguing line shifts and intensity variations that our model predicts and which are observed experimentally. On closer inspection, there are clear indications of additional small mixing with other vibrational or rotational modes, not included in our model, that lead to minor frequency shifts and fractionation of spectral lines. In stark contrast, the pseudorotation has a profound effect on state mixing in the region of the CH stretches. An individual CH stretch can approximately move between equatorial and axial configurations over the course of the pseudorotation and this leads to larger couplings that are found for the scissors, and these larger couplings lead to substantial state mixing.

The present study does not include coupling to the radial degree of freedom associated with pseudorotation. Bauman and Laane<sup>3</sup> carefully considered this coupling, and, based on their work, we believe that its inclusion is essential for a more detailed understanding of higher resolution details of the CH<sub>2</sub> scissor fundamental.

## SUPPLEMENTARY MATERIAL

See the [supplementary material](#) for the symmetrized Hamiltonian matrices for the CH stretches and CH<sub>2</sub> overtone and combination states as well as additional equations describing the derivation of the CH stretch dipole moment matrix elements.

## ACKNOWLEDGMENTS

E.L.S. acknowledges support from NSF via Grant No. CHE-1900095 and useful conversations with Zachery Dyott. We thank J. Sorensen for recording the cyclopentane spectra. The NASA Outer Planets Research and Planetary Data Archiving and Restoration Tools program (PDART) provided funding through Grant No. 80NSSC19K0417.

## AUTHOR DECLARATIONS

### Conflict of Interest

The authors have no conflicts to disclose.

## DATA AVAILABILITY

The data that support the findings of this study are available within the article and its [supplementary material](#).

## REFERENCES

- 1 J. E. Kilpatrick, K. S. Pitzer, and R. Spitzer, "The thermodynamics and molecular structure of cyclopentane," *J. Am. Chem. Soc.* **69**, 2483–2488 (1947).
- 2 T. H. Chao and J. Laane, "Vibrational studies of cyclopentane - effect of 10-fold barrier to pseudorotation," *J. Mol. Spectrosc.* **70**, 357–360 (1978).
- 3 L. E. Bauman and J. Laane, "Pseudorotation of cyclopentane and its deuterated derivatives," *J. Phys. Chem.* **92**, 1040–1051 (1988).
- 4 R. A. MacPhail and J. E. Variyar, "Pseudorotation dynamics in liquid cyclopentane by Raman spectroscopy," *Chem. Phys. Lett.* **161**, 239–244 (1989).
- 5 J. E. Variyar and R. A. MacPhail, "Pseudorotation and the Raman CH stretching spectrum of gaseous cyclopentane-*d*<sub>9</sub> - local modes in a floppy molecule," *J. Phys. Chem.* **96**, 576–584 (1992).
- 6 X. Pan and R. A. MacPhail, "A Raman study of cyclopentane-*d*<sub>9</sub> pseudorotation dynamics as a function of pressure," *Chem. Phys. Lett.* **212**, 64–70 (1993).
- 7 P. Kowalewski, H.-M. Frey, D. Infanger, and S. Leutwyler, "Probing the structure, pseudorotation, and radial vibrations of cyclopentane by femtosecond rotational Raman coherence spectroscopy," *J. Phys. Chem. A* **119**, 11215–11225 (2015).
- 8 H. L. Strauss, "Pseudorotation - a large-amplitude molecular-motion," *Annu. Rev. Phys. Chem.* **34**, 301–328 (1983).
- 9 A. F. Sax, "On pseudorotation," *Chem. Phys.* **349**, 9–31 (2008).
- 10 E. G. Buchanan, J. C. Dean, T. S. Zwier, and E. L. Sibert, "Towards a first-principles model of Fermi resonance in the alkyl CH stretch region: Application to 1,2-diphenylethane and 2,2,2-paracyclophane," *J. Chem. Phys.* **138**, 064308 (2013).
- 11 N. M. Kidwell, D. N. Mehta-Hurt, J. A. Korn, E. L. Sibert, and T. S. Zwier, "Ground and excited state infrared spectroscopy of jet-cooled radicals: Exploring the photophysics of trihydronaphthyl and inden-2-ylmethyl," *J. Chem. Phys.* **140**, 214302 (2014).
- 12 D. P. Tabor, D. M. Hewett, S. Bocklitz, J. A. Korn, A. J. Tomaine, A. K. Ghosh, T. S. Zwier, and E. L. Sibert, "Anharmonic modeling of the conformation-specific IR spectra of ethyl, n-propyl, and n-butylbenzene," *J. Chem. Phys.* **144**, 224310 (2016).
- 13 K. N. Blodgett, D. Sun, J. L. Fischer, E. L. Sibert, and T. S. Zwier, "Vibronic spectroscopy of methyl anthranilate and its water complex: Hydrogen atom dislocation in the excited state," *Phys. Chem. Chem. Phys.* **21**, 21355–21369 (2019).
- 14 P. F. Bernath, D. M. Bittner, and E. L. Sibert III, "Isobutane infrared bands: Partial rotational assignments, ab initio calculations, and local mode analysis," *J. Phys. Chem. A* **123**, 6185–6193 (2019).
- 15 P. F. Bernath, E. L. Sibert III, and M. Dulick, "Neopentane vibrations: High resolution spectra and anharmonic calculations," *J. Phys. Chem. A* **124**, 3438–3444 (2020).
- 16 P. F. Bernath and E. L. Sibert III, "Cyclohexane vibrations: High-resolution spectra and anharmonic local mode calculations," *J. Phys. Chem. A* **124**, 9991–10000 (2020).
- 17 I. M. Mills, "Infra-red and Raman selection rules for cyclopentane," *Mol. Phys.* **20**, 127–138 (1971).
- 18 M. B. Dawadi and D. S. Perry, "Communication: Conical intersections between vibrationally adiabatic surfaces in methanol," *J. Chem. Phys.* **140**, 161101 (2014).
- 19 J. J. Sorensen, P. F. Bernath, R. M. Johnson, R. Dodangodage, W. D. Cameron, and K. LaBelle, "Absorption cross sections of n-butane, n-pentane, cyclopentane and cyclohexane," *J. Quant. Spectrosc. Rad. Transfer* (submitted).
- 20 D. P. Tabor, R. Kusaka, P. S. Walsh, E. L. Sibert, and T. S. Zwier, "Isomer-specific spectroscopy of benzene-(H<sub>2</sub>O)<sub>n</sub>, n = 6, 7: Benzene's role in reshaping water's three-dimensional networks," *J. Phys. Chem. Lett.* **6**, 1989–1995 (2015).
- 21 E. L. Sibert, "Modeling vibrational anharmonicity in infrared spectra of high frequency vibrations of polyatomic molecules," *J. Chem. Phys.* **150** (2019).
- 22 C. R. Jacob and M. Reiher, "Localizing normal modes in large molecules," *J. Chem. Phys.* **130**, 084106 (2009).
- 23 T. Weymuth, C. R. Jacob, and M. Reiher, "A local-mode model for understanding the dependence of the extended amide III vibrations on protein secondary structure," *J. Phys. Chem. B* **114**, 10649–10660 (2010).
- 24 E. L. Sibert, "Dressed local mode Hamiltonians for CH stretch vibrations," *Mol. Phys.* **111**, 2093–2099 (2013).

<sup>25</sup>X. Cheng and R. P. Steele, "Efficient anharmonic vibrational spectroscopy for large molecules using local-mode coordinates," *J. Chem. Phys.* **141**, 104105 (2014).

<sup>26</sup>X. Cheng, J. J. Talbot, and R. P. Steele, "Tuning vibrational mode localization with frequency windowing," *J. Chem. Phys.* **145**, 124112 (2016).

<sup>27</sup>P. M. Zimmerman and P. Smereka, "Optimizing vibrational coordinates to modulate intermode coupling," *J. Chem. Theory Comput.* **12**, 1883–1891 (2016).

<sup>28</sup>M. J. Frisch, G. W. Trucks, H. B. Schlegel, G. E. Scuseria, M. A. Robb, J. R. Cheeseman, G. Scalmani, V. Barone, G. A. Petersson, H. Nakatsuji *et al.*, Gaussian 16 Revision C.01," Gaussian Inc., Wallingford, CT, 2016.

<sup>29</sup>B. Fehrens, D. Luckhaus, M. Quack, M. Willeke, and T. R. Rizzo, "Ab initio calculations of mode selective tunneling dynamics in <sup>12</sup>CH<sub>3</sub>OH and <sup>13</sup>CH<sub>3</sub>OH," *J. Chem. Phys.* **119**, 5534–5544 (2003).